Ocean Modelling 28 (2009) 250–265

Contents lists available at ScienceDirect

Ocean Modelling

journal homepage: www.elsevier.com/locate/ocemod

Application of a vanishing, quasi-sigma, vertical coordinate for simulation of high-speed, deep currents over the Sigsbee Escarpment in the Gulf of Mexico

Dmitry S. Dukhovskoy [a,*], Steven L. Morey [a], Paul J. Martin [b], James J. O'Brien [a], Cortis Cooper [c]

[a] Center for Ocean – Atmospheric Prediction Studies, The Florida State University, 2035 E. Paul Dirac Drive, R.M. Johnson Bldg. – Suite 200, Tallahassee, FL 32306-2840, USA
[b] Naval Research Laboratory, Stennis Space Center, MS 39529, USA
[c] Energy Technology Co., Chevron, 6001 Bollinger Canyon Rd, Rm L-4240, San Ramon, CA 94583, USA

ARTICLE INFO

Article history:
Received 25 September 2008
Received in revised form 26 January 2009
Accepted 23 February 2009
Available online 3 March 2009

Keywords:
Numerical models
Deep currents
Topographic waves
Numerical truncation error
Vertical discretization
Sigsbee Escarpment
Gulf of Mexico

ABSTRACT

Recent observations over the Sigsbee Escarpment in the Gulf of Mexico have revealed extremely energetic deep currents (near 1 m s^{-1}), which are trapped along the escarpment. Both scientific interest and engineering needs demand dynamical understanding of these extreme events, and can benefit from a numerical model designed to complement observational and theoretical investigations in this region of complicated topography. The primary objective of this study is to develop a modeling methodology capable of simulating these physical processes and apply the model to the Sigsbee Escarpment region. The very steep slope of the Sigsbee Escarpment (0.05–0.1) limits the application of ocean models with traditional terrain-following (sigma) vertical coordinates, which may represent the very complicated topography in the region adequately, can result in large truncation errors during calculation of the horizontal pressure gradient. A new vertical coordinate system, termed a vanishing quasi-sigma coordinate, is implemented in the Navy Coastal Ocean Model for application to the Sigsbee Escarpment region. Vertical coordinate surfaces for this grid have noticeably gentler slopes than a traditional sigma grid, while still following the terrain near the ocean bottom. The new vertical grid is tested with a suite of numerical experiments and compared to a classical sigma-layer model. The numerical error is substantially reduced in the model with the new vertical grid. A one-year, realistic, numerical simulation is performed to simulate strong, deep currents over the Escarpment using a very-high-resolution nested modeling approach. The model results are analyzed to demonstrate that the deep-ocean currents in the simulation replicate the prominent dynamical features of the observed intense currents in the region.

1. Introduction

Observations of currents in the deep Gulf of Mexico have shown that the abyss is far from quiescent. Strong near-bottom currents exceeding 1 m s^{-1} have been measured in water depths of 2000 m over the Sigsbee Escarpment (SE), south of New Orleans (Hamilton and Lugo-Fernandez, 2001; Hamilton et al., 2003). Evidence of extreme deep currents in the region, potentially important for offshore petroleum exploration and extraction activities, has led to intensive observational efforts in the area (discussed in Section 2) and has sparked interest within the oceanographic community (Hamilton, 1990; Hamilton and Lugo-Fernandez, 2001; Oey and Lee, 2002; Hamilton, 2007).

Despite a growing database of deepwater current measurements and analyses of the observations, mechanisms generating the deep strong currents remain unclear. It has been speculated that intensification of currents along a steep slope is a manifestation of topographic Rossby waves (TRWs, Rhines, 1970) propagating along the isobaths such that the shallow water is to the right (Hamilton, 1990). The mechanisms generating these TRWs are unclear. The waves may be excited by interactions of energetic mesoscale circulation features with topography. The energetic circulation features are a product of the Loop Current, a branch of the North Atlantic's western boundary current that dominates the basin-scale circulation in the Gulf of Mexico. The Loop Current enters the Gulf through the Yucatan Strait and leaves the Gulf through the Straits of Florida (Fig. 1a). The Loop Current flows clockwise with near-surface velocities more than 0.8 m s^{-1} making a loop that extends northward. The Loop Current sheds anticyclonic mesoscale eddies (Loop Current eddies) that drift westward with smaller scale cyclones, called frontal eddies, along their periphery (the circulation in the Gulf is analyzed in detail in the literature, e.g., Sturges and Lugo-Fernandez, 2005). It is hypothesized that variations in the position of the front of the Loop Current, Loop Current eddy shedding events, and the propagation of Loop Current eddies and their associated smaller cyclones across the Gulf of Mexico generate the TRWs over the deep continental slope

* Corresponding author. Tel.: +1 850 644 1168; fax: +1 850 644 4841.
E-mail addresses: ddmitry@coaps.fsu.edu (D.S. Dukhovskoy), smorey@coaps.fsu.edu (S.L. Morey), paul.martin@nrlssc.navy.mil (P.J. Martin), jobrien@coaps.fsu.edu (J.J. O'Brien), cortcooper@chevron.com (C. Cooper).

1463-5003/$ - see front matter © 2009 Elsevier Ltd. All rights reserved.
doi:10.1016/j.ocemod.2009.02.009

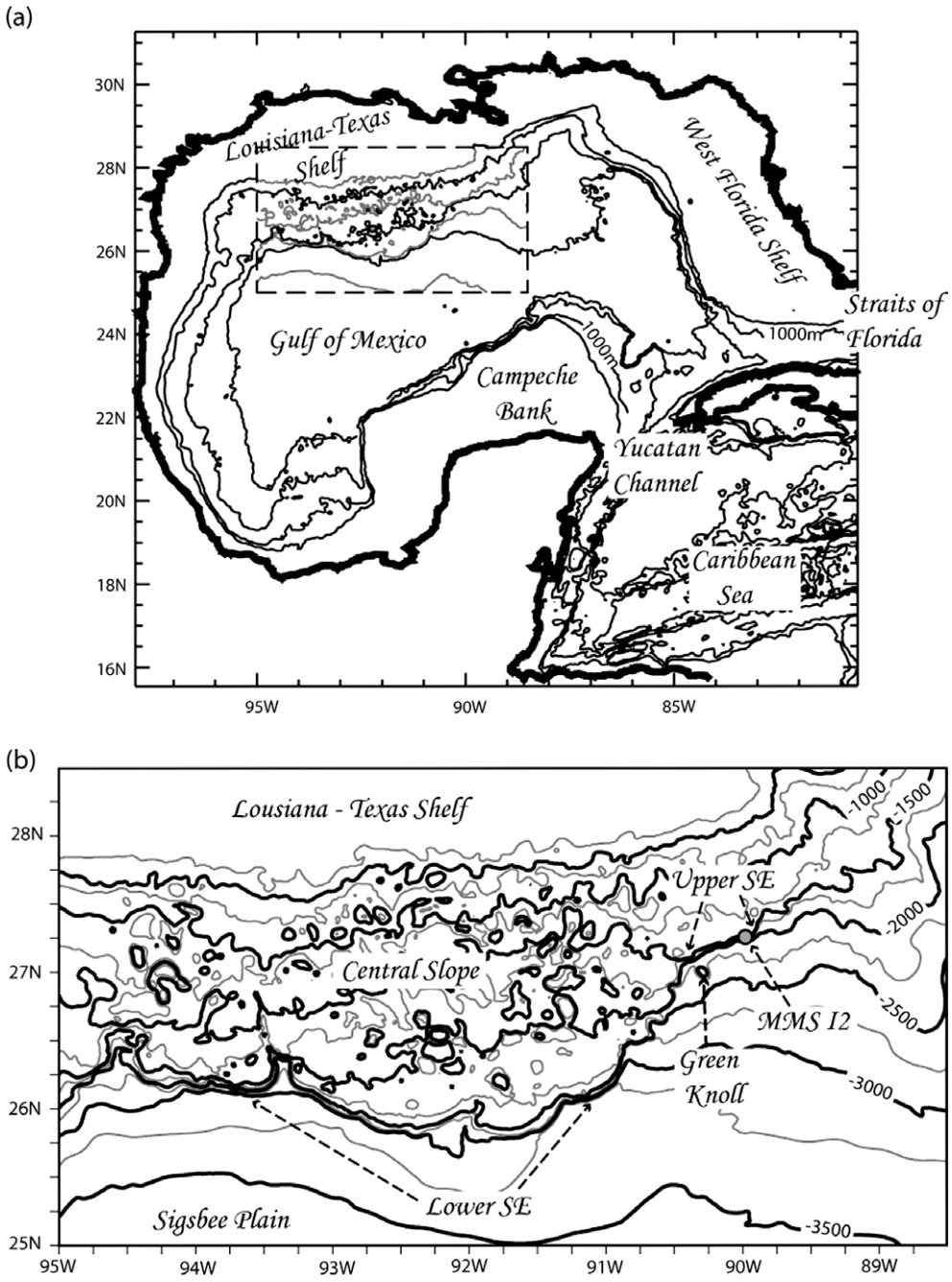

Fig. 1. (a) Bathymetry of the Gulf of Mexico model domain. Bathymetry contours are drawn every 1000 m. The Sigsbee Escarpment high-resolution model domain is indicated with a rectangle, and bathymetry contours in this area are drawn every 500 m. (b) Bathymetry of the Sigsbee Escarpment model domain. Bathymetry contours are drawn every 250 m. The location of the MMS I2 mooring is indicated in the lower panel.

responsible for the deep strong currents observed over the Sigsbee Escarpment (Hamilton and Lugo-Fernandez, 2001; Oey and Lee, 2002).

Although previous studies suggest that strong events over the SE are a manifestation of TRWs, this idea has to be revisited and validated and alternative hypotheses should be considered. For example, recent observations suggest that strong currents along the SE could be related to deep eddies impinging upon the slope (Donohue et al., 2006). Other key questions concerning the deep-water dynamics remain unanswered, and include: Are strong currents in the deep Gulf of Mexico dynamically uncoupled from the upper-ocean currents? What governs the periodicity of the energetic currents? Are wave-like motions over the deeper western part of the SE dynamically related to the upper SE further to the northeast?

A suitable model of the SE could help in addressing all of these questions. Observational studies have shown that the SE strongly influences the local deep dynamics and resulting current patterns (Donohue et al., 2006). Thus, it is envisioned that an appropriate model of the SE should have accurate representation of the bottom topography. The model should have very fine resolution for representing the steep slope because the SE is roughly 10-km wide at the narrowest places, with vertical extents of 500–1000 m. Due to the extremely complex bottom topography in the area and the very steep slope of the SE, developing a model of this region is challenging and has numerical issues that must be addressed.

Several ocean models have been used to study the deep-ocean dynamics in the region. However, the models have not had high enough resolution as well as sufficiently accurate topographic representation to simulate the near-bottom strong currents and the physical processes responsible for these events. Not only has vertical resolution near the ocean bottom been too coarse in most models, but terrain-following coordinate models have required smoothed topography and models with geopotential coordinates typically have stepped topography and cannot properly simulate the propagation of the features (Dukhovskoy et al., 2006). Terrain-following (sigma) coordinates permit accurate representation of bottom topography, but over steep slopes, sigma layers become strongly inclined, which causes numerical truncation errors when calculating horizontal gradients in a baroclinic ocean (Haney, 1991). Substantial efforts have been undertaken to overcome the pressure-gradient problem in sigma-coordinate models. A number of approaches and numerical algorithms that reduce this error have been developed including the use of higher order approximations (Mihailović and Zanjic, 1984; Chu and Fan, 1997), weighed Jacobian methods (Shchepetkin and McWilliams, 2003), reduction of anisotropy in sigma-coordinate models (Thiem and Berntsen, 2006), calculation of the pressure gradient from the density interpolated to z-levels (Stelling and Van Kester, 1994) and others (see overview in Ezer et al., 2002). While some methods exhibit error reduction over sloping bottom, it is not clear how they would perform over very steep topography.

In some cases in order to reduce the error, the bottom topography is heavily filtered as in the model studies by Oey (1996) and Oey and Lee (2002) which addressed the problem of TRWs in the deep Gulf of Mexico. In the latter study, the horizontal grid spacing of the Princeton Ocean Model simulation used in the experiments was ~5 km in the northern Gulf of Mexico with 25 sigma layers. The primary objective of these studies was to examine TRWs over gentle topographic slopes in the north-central Gulf near the 3000-m isobath. The studies did not attempt to analyze currents over steep regions such as SE due to insufficient resolution in the model (Oey and Lee, 2002).

The objective of this study is to develop a model of the Sigsbee Escarpment capable of simulating dynamical processes and energetic bottom-intensified currents with characteristics similar to those observed. It is envisioned that the methodology developed here can eventually serve as a tool for exploring the deep-ocean dynamics in the region. For this purpose, the Navy Coastal Ocean Model (NCOM) with a Generalized Vertical Coordinate is employed (Section 3). A "vanishing quasi-sigma" vertical coordinate system is developed exploiting the flexibility of the NCOM vertical grid. This vertical coordinate system allows accurate representation of topography in the model with significantly reduced numerical truncation errors (Section 4). The implementation of the new vertical grid is tested within the SE domain prior to performing a realistic one-year integration to simulate events of high-speed, near-bottom currents over the escarpment. The results are analyzed and compared to the observed characteristics of the energetic events over the Sigsbee Escarpment (Section 5).

2. Background

2.1. Description of the region

The SE is located at the offshore edge of the Central Slope south of the Louisiana-Texas Shelf where the seafloor drops dramatically to the Sigsbee Plain of the Gulf of Mexico Basin (Fig. 1). The local maxima of the bottom slope in the region define the SE, and in the model topography described below, it locally exceeds 0.15. The SE cannot be defined based on a particular isobath because the depth of the escarpment increases toward the southwest. The escarpment north of roughly 26.8°N and east of 90.5°W drops from around 1400 m to a depth of about 2200 m. To the south of 26.4°N and west of approximately 90.8°W, the seafloor drops abruptly from about 2400 m to a depth of 3400 m. For the purposes of this work, these depth ranges will define the upper (eastern) SE and lower (western) SE, respectively (Fig. 1). The SE, both upper and lower regions, appear in maps of topographic contours as a convergence of isobaths to the west of the Mississippi Fan region.

2.2. Historical observations of deep currents in the Gulf of Mexico

Before the 1960s, it was generally assumed that very weak or no currents exist in the deep ocean (Skoda, 1970). In the late 1950s, indirect evidence (e.g., photographs of the deep-ocean bottom with ripple marks, scour around stones, and current lineations (Hunkins et al., 1960; Hollister and Heezen, 1966)) suggested the possibility of the existence of strong, near-bottom currents in the abyss and excited interest in this topic among oceanographers (e.g., Rowe and Menzies, 1968; Reid, 1969).

Probably the first evidence of strong bottom currents in the deep Gulf of Mexico was presented by Pequegnat (1972), who reported substantial velocities up to 0.19 m s^{-1} from direct current measurements at the Mississippi Cone at depths of 3000–3300 m. Later, in the mid-1980s, currents of up to 0.3 m s^{-1} were measured over the lower continental slope and deep basin of the Gulf of Mexico (Hamilton, 1990). Hamilton (1990) advocates that low-frequency velocity fluctuations observed in the time series could be attributed to TRWs. Estimated periods of the TRWs are 25 days and 40–100 days, with wavelengths of about 150–250 km.

Strong currents near the bottom over the SE were found in observations conducted by the US Department of the Interior Minerals Management Service (MMS) during a four-year, exploratory study of deepwater currents in the Gulf of Mexico (Nowlin et al., 2001; Donohue et al., 2006). The observations were supplemented by measurements from moorings deployed in the study area by the DeepStar Consortium and Louisiana State University. The depth of the bottom current-meters varied from approximately 10 to 100 m above the local bottom. Two years of current observations were collected from August 1999 to August 2001 at the upper portion of the SE in the vicinity of Green Knoll (Fig. 1b). These measurements are analyzed in Hamilton and Lugo-Fernandez (2001) and Nowlin et al. (2001). Bottom-intensified currents exceeding 0.85 m s^{-1} were recorded 11 m above the bottom at the I2 mooring (27° 13.683′N 89° 58.264′W, location is shown in Fig. 1b) several times during this period. Hamilton (2007) indicated that the upper- and lower-level flows are decoupled, but speculated that in some instances there seems to be connection between the upper-layer flows and the currents in the lower layer. Further observations of the SE region have not provided conclusive evidence of the importance of a dynamical linkage of the upper and lower layers over the SE (Donohue et al., 2006).

During February 2003–April 2004, an array of moorings was deployed in the area. Within this time frame, a number of floats (neutrally buoyant and profiling floats) were launched in the region. A mesoscale-resolving array of 27 inverted echo sounders with pressure gauges (Hamilton et al., 2003) was deployed to enable a quantitative mapping of the regional circulation. The observations have revealed extraordinary inhomogeneity in the dynamics over the SE. Currents at the upper (eastern) portion of the SE differ in character and energy from currents at the lower (western) portion of the SE (Donohue et al., 2006). Near-bottom mean currents (calculated from one-year records at 100 m above the bottom) show enhanced southwestward flow along the SE. These currents are persistent in their direction and rarely reverse. The mean deep currents calculated from the MMS observations range from 0.05 to 0.3 m s^{-1} (Fig. 4.2–13, in Donohue et al., 2006). A particularly strong mean

current of about 0.1 m s^{-1} is noticeable at the eastern part of the lower SE (~26°N 91.5°W). At the upper SE, a local maximum of the mean current is observed at the eastern end of the escarpment where the isobaths converge (27–27.3°N, 89.2–89.9°W). Over the shallower depths to the north of the escarpment, the mean currents are mostly weaker revealing the insulating effect of the steep slope (Donohue et al., 2006). Estimated from the observations, the standard deviation (STD) ellipses of the mean current vectors along the SE have major axes that are rotated at small angles to the isobaths. Over the less steep slope, the ellipses are more circular and the major axes are oriented at greater angles to the isobaths.

Extreme events over the escarpment are episodic in time and localized in space. Analysis of the measurements suggests that during 2003–2004 the deep currents were in the upper quartile of their speed range in only 0.5–1.5% of the records (Donohue et al., 2006). Regions of maximum and minimum speed of the currents can be close to each other along the escarpment. Hamilton (2007) has noticed drastically different current speeds measured at the upper SE at two moorings 6 km apart. At the I2 mooring location (shown in Fig. 1b), recorded currents at 11 m above the bottom exceeded 0.7 m s^{-1}, with speeds occasionally approaching 1 m s^{-1}. The speeds at the other mooring located 6 km to the west along the slope were approximately half of those at the I2 location. During March 2003–March 2004, the maximum speeds observed in the area were not as extreme as those measured by the September 1999 I2 mooring. The maximum currents measured at instruments from 100 to 500 m above the bottom were mostly concentrated in two locations: one at the upper SE (~27–27.5°N, 89.2–90.2°W) with speeds of 0.5–0.6 m s^{-1}, and the other at the lower SE (~26–26.3°N, 90.8–91.3°W) with currents of 0.4–0.5 m s^{-1}. Intensification of the currents in the lower part of the water column as reported in Hamilton and Lugo-Fernandez (2001) has also been observed during these observations (Hamilton, 2007). In these current profiles, however, a reduction of speed near the bottom is evident and likely due to a frictional bottom boundary layer resulting in the maximum speeds occurring at some distance above the bottom. For example, the greatest mean speed in the deep layer measured at a mooring over the lower SE (~91°W, 26°N) was 200 m above the bottom (Donohue et al., 2006).

Spectral analyses of the velocity time series have identified the ranges of predominant periodicities of the low-frequency oscillations over the SE. Kinetic energy spectra of the velocity records do not have a well defined peak, but the energy is concentrated within a wide frequency range. Periodicities of the fluctuations depend on the location of the records, both the east–west position along the escarpment and the depth. Typically, the estimated time scales of the deep, low-frequency motions in the region vary from 10 to 40 days (Hamilton and Lugo-Fernandez, 2001; Donohue et al., 2006; Hamilton, 2007).

2.3. Prominent features of the deep-ocean dynamics over the SE

Based on the historical observations, a fundamental set of prominent features are identified. It is expected that for a model to be deemed useful for studying these dynamics, it should be able to reproduce these characteristics of the deep currents in the region about the SE:

Mean currents. Along the SE the near-bottom mean currents are directed dominantly southwestward. Speeds of the mean currents range from 0.05 to 0.3 m s^{-1}. The mean currents are weaker over the shallower (upper) part of the SE. Along the slope, intensification of the mean currents is observed at the eastern sides of the lower and upper SE. The major axes of the STD ellipses are oriented at small angles to the isobaths over the escarpment.

Extreme events. Episodic extreme events affect the SE with maxima occurring just below or on the escarpment in two separate regions, one near the eastern end of the upper SE (~89.5–90°W, 27–27.3°N) and the other over the eastern lower SE (91–91.2°W, 26–26.2°N). At the upper SE, speeds of the observed extreme currents have been measured in the range of 0.6 to greater than 1 m s^{-1}. At the lower SE, observed maximum speeds over 0.65 m s^{-1} have been observed.

Time scales of deep currents. The estimated periodicity of the low-frequency oscillations in the velocity records over the SE is 10–40 days with some longer periods up to 100 days.

3. Numerical model description and simulations

3.1. The Navy Coastal Ocean Model

All numerical simulations used for this project are applications of the Navy Coastal Ocean Model (NCOM) (Martin, 2000), developed at the U.S. Naval Research Laboratory for operational applications. Specifically, the NCOM Version 3.2 code is used. The NCOM is a primitive-equation, three-dimensional, ocean model with the hydrostatic and Boussinesq approximations. The model uses an Arakawa C staggered grid. It has several numerical differencing and integration options. For this study, second-order-centered averages and differencing methods are used for spatial interpolation and approximation of spatial derivatives, with the leapfrog semi-implicit method used for time integration. The bottom friction used in the simulation is parameterized with a quadratic drag law and implicitly calculated by the model. The drag coefficient c_b is calculated as

$$c_b = \max\left\{\frac{K^2}{\ln^2\left(\frac{\Delta z_b}{2z_0}\right)}, c_{b\min}\right\} \quad (1)$$

Where, K is Von Karman's constant, c_{bmin} is the minimum value that the bottom drag coefficient can attain (set at 0.0025 in this study), Δz_b is the height of the bottom grid cell and z_0 the bottom roughness (in this study $z_0 = 0.01$ m).

The NCOM belongs to a class of hybrid-vertical-coordinate ocean models. Early versions of the NCOM combine geopotential (z-level) coordinates with terrain-following (sigma) coordinates. The sigma coordinates are specified as a fraction of the total water-column depth from the free surface to either the ocean bottom, or in the case of the NCOM's hybrid vertical grid, some specified depth level if the ocean bottom is deeper. The σ coordinates need not be equally spaced and can be stretched. The z-levels are at fixed depths below a resting ocean surface (geopotential) and the ocean model topography is rounded at each horizontal point to the nearest z-level. The use of z-levels, while eliminating the pressure-gradient error of sigma-coordinate models (Mellor et al., 1994, 1998), results in a step-like representation of topography and presents complications when higher resolution is desired near the ocean bottom. Dukhovskoy et al. (2006) showed that topographic Rossby waves cannot be simulated properly in a z-level model unless a large number of levels are used so that the size of the topographic steps are reduced to form a reasonably accurate representation of the topography.

NCOM Versions 3.1 and later feature a new extension to the hybrid vertical grid, termed by the model developers as a Generalized Vertical Coordinate (GVC). This new vertical coordinate system offers traditional sigma coordinates (that can vary in time as the total water-column depth changes due to free-surface deviations), fixed depth (or static) coordinates with vertical distributions varying as a function of horizontal location, traditional z-level coordinates, or

z-level grids with shaving of the bottom grid cell to match the realistic topography. Additionally, grid cells, even on the sigma grid, can be masked out so they are not active grid cells. The generalized nature of the vertical coordinate system allows for great flexibility, which has been exploited for this study through the development of what will be termed vanishing quasi-sigma (VQS) coordinates.

3.2. Vanishing quasi-sigma vertical coordinate

The VQS grid is defined as a function of the local depth of the ocean bottom. As the ocean becomes shallower, the number of active, sigma-type coordinates is reduced. That is, the deepest coordinates "vanish" as they are masked out (Fig. 2a and d). The grid is generated as follows. A sequence of reference vertical grids is generated for specified (increasing) bottom depths. Each reference vertical grid is computed using a uniform (linear) stretching function to provide higher resolution near the bottom and the surface (Fig. 2b). The stretching parameter is defined through interval halving iteration until the thickness of the bottom and surface layers do not exceed desired values (<15 m in this study). The reference vertical grids have different numbers of vertical layers (increasing with depth) for given depths and specified stretching factors. For a model grid point (i, j) with a specific depth $h(i, j)$ the two reference grids corresponding to reference depths above and below $h(i, j)$ are identified. The vertical grid is computed for that point using linear weighing of the two reference grids. The minimum bottom layer vanishes when it becomes thinner than a specified threshold value (3 m in this study). The generated grid is forced to maintain a minimum number of layers (10 in this study) in shallow regions, where the layer thicknesses may be less than 3 m.

The VQS scheme has the benefit of allowing for the vertical grid to closely follow the ocean bottom slope, but restricts the depth range for a given coordinate surface reducing its slope near steep topographic features when compared to the classic sigma-coordinate application (Fig. 2a and c). Reducing the slopes of the sigma-coordinate surfaces reduces the numerical truncation errors (demonstrated in the following sections), which in classic sigma models can be done by reducing the slope of the escarpment (without increasing the horizontal resolution).

3.3. Application of the NCOM to the Sigsbee Escarpment region

To achieve the very high resolution necessary for properly resolving the SE and simulating the impacts of larger-scale circulation features on the region, a two-level nested modeling system is applied using the NCOM. Two model domains are configured for this nested approach using the VQS vertical grid. The outer domain

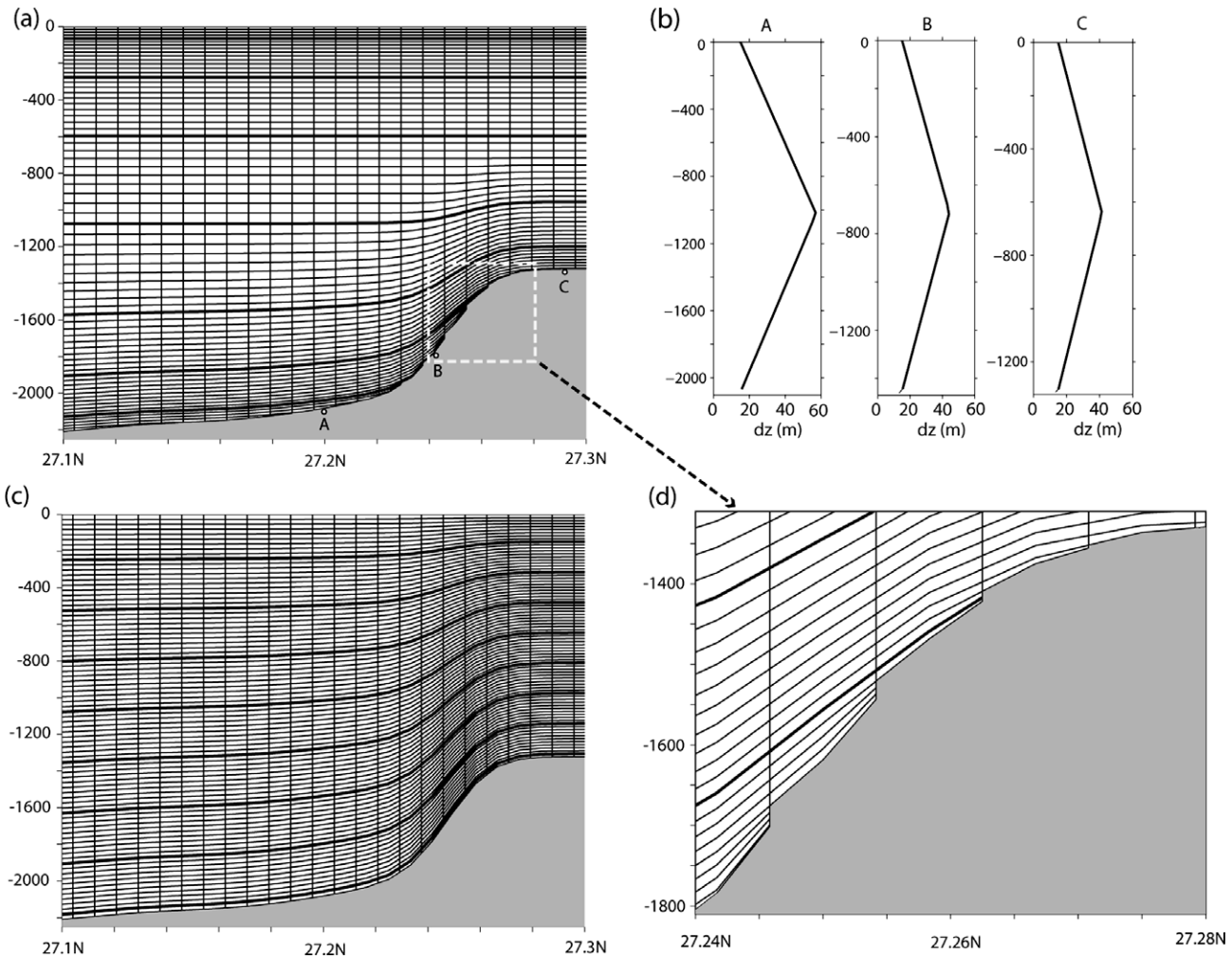

Fig. 2. (a) Vertical coordinate surfaces along 90°W from the high-resolution SE model using the VQS coordinate system. Every 10th coordinate surface is highlighted for clarity. A rectangle indicates the region shown in (d). (b) Vertical grid spacing (m) versus depth at three locations (shown by bullets in (a)). (c) An evenly stretched traditional sigma grid with 80 layers is shown (used in test runs). Note in the traditional grid strong inclination of sigma surfaces over steep slopes through the water column as well as overburdening of the shallow region with sigma layers. (d) Magnification of the VQS coordinate grid bounded by the rectangle in (a).

is a 1/20° horizontal resolution (in latitude and longitude between like variables on the Arakawa C grid) encompassing the entire Gulf of Mexico and northwestern Caribbean (GoM domain, Fig. 1a). Next is a SE domain with a 30 arc second (1/120°) grid (Fig. 1b) and is focused on the region surrounding the escarpment. The outer GoM model domain is integrated for several (10) years to simulate the Loop Current and the mesoscale eddy field of the GoM and to choose an appropriate case for a high-resolution nested model simulation of the SE. One particular year with intensified Loop Current Eddy activity over the SE region in the GoM model domain is identified as a case for which to run the nested SE model experiment.

3.3.1. Gulf of Mexico domain

Circulation of the Gulf of Mexico and northwestern Caribbean is simulated in a model domain encompassing the region 98.15°W to 80.6°W and 15.55°N to 31.5°N (Fig. 1a). The eastern boundary is open in the Caribbean Sea and Florida Strait, and a small part of the southern boundary extending over the shallow Nicaragua Shelf has been artificially closed. The northern and western boundaries are naturally closed. The topography for the model is derived from the NOAA ETOPO2 2-min-resolution data set with some regional editing and interpolated to the model grid before applying a 9-point box average twice. The simulation domain and forcing are based on that described in Morey et al. (2003).

The vertical grid is configured as follows. Below the free surface (the first vertical grid level), 10 static sigma layers are evenly spaced in the upper 150 m. Thus the top-most layer varies its thickness with the free ocean surface. Below 150 m, the VQS grid is applied with a maximum of 50 additional layers (yielding a total of up to 60 vertical layers).

The model is initialized at rest with temperature and salinity interpolated from the World Ocean Atlas 1998 (WOA98) January climatology (Conkright et al., 1998). Surface boundary conditions for momentum and temperature are obtained from the DaSilva et al. (1994) monthly-climatological heat and radiative fluxes and wind stresses. A salinity flux is prescribed to be constant in space and time to balance the annual average fresh water input by the thirty rivers in the model domain. The rivers are treated as mass sources of fresh water with flow rates derived from monthly-climatological USGS data or other sources for Mexican rivers. Open boundary conditions are obtained by adjusting the baroclinic flow field at the boundary to the WOA98 average temperature and salinity field. This forces the incoming Caribbean Current and exiting Florida Current, producing a mean Yucatan Channel transport of 26 Sv.

Integrating the model from its initial state, a Loop Current is rapidly formed. The first Loop Current Eddy is shed in the sixth month of integration. The model is integrated for 10 years for analysis. The Loop Current penetration and eddy shedding behavior is similar to observations reported in prior studies. For example, the average period between Loop Current Eddy separations from 8 years of model data is 10.2 months, varying between 4 and 22 months. This can be compared to the Sturges and Leben (2000) estimate from satellite observations of 9.5 months, varying between 3 and 17 months, and Leben's (2005) estimate of 9.4 months from 16 altimetry-observed, eddy-separation events.

3.3.2. High-resolution Sigsbee Escarpment domain

A second model domain is configured to include the SE region and surrounding Gulf of Mexico waters from 95°W to 88° 30.5′W and 25°N to 28°29.5′N (Fig. 1b). The horizontal resolution of the model grid is 30 arc seconds (1/120°). Topography is derived from the NOAA NODC 30-arc-second gridded Coastal Relief and Digital Elevation Map, with a nine-point centered-average filter applied three times to the bathymetric data set prior to use in the model. The bathymetry is blended with the coarser-resolution GoM 1/20° model topography near the edges of the domain so that the two topographies match at the boundaries. The vertical grid has a maximum of 80 layers and is configured with the VQS grid (described in Section 3.2) (Fig. 2a). The thickness of the bottommost grid cell is between 3 and 15 m.

The high-resolution SE model is nested within the larger-scale GoM model and run for one year selected from the 10-year GoM integration. Initial fields (temperature, salinity, currents, and sea-surface elevation) and boundary conditions are interpolated from the GoM model to the fine-resolution grid. Coupling is one-way in that outgoing information is simply radiated away and does not feed back into the large-scale model. For this realistic simulation, the same surface fluxes applied to the GoM model domain are used to force the nested SE model domain. Prior to conducting the realistic simulation model experiments, test model runs are performed with the SE model domain as described in Section 4.2 to evaluate the performance of the new VQS grid.

4. Evaluation of the VQS vertical coordinate system

4.1. Sigma-coordinate pressure-gradient errors

The manner in which the new vertical grid is defined distinguishes it from the classic sigma-coordinate system while preserving certain useful features of the sigma coordinate. The conventional definition of sigma (σ) coordinates in two dimensions is

$$\sigma = \frac{z - \eta(x,t)}{H(x) + \eta(x,t)} \tag{2}$$

where (x, z) are the horizontal and vertical Cartesian coordinates, H is the water-column depth below a resting free surface ($z = 0$), and η is the free-surface deviation at time t. Coordinate transformation (2) defines surfaces such that the bottom surface follows the terrain (thus called "terrain-following") and the upper surface matches the sea surface. In a sigma-coordinate ocean model, sigma surfaces define the upper and lower interfaces of volume elements within the sigma layers, but their depths can change in time with variations in the sea surface. Hence, the vertical model layers coincide with the vertical sigma layers (Fig. 2c). Within a fixed vertical layer k, the sigma coordinate does not change horizontally:

$$\left.\frac{\partial \sigma}{\partial x}\right)_k = 0. \tag{3}$$

In the VQS coordinate system, as in classic sigma coordinates, the bottom surface follows the terrain, the top-most surface follows the free surface of the ocean, and the depths of interior coordinate surfaces are computed as fractions of the total water-column depth. These fractions, however, are not fixed over the domain but are allowed to vary at each horizontal grid point, and the total number of vertical levels also varies with the seafloor depth. Thus, the VQS coordinate is defined algorithmically as described in Section 3.2 as opposed to a simple analytical expression like (2). A key difference is that in the VQS vertical coordinate system, the vertical coordinate surfaces can intersect surfaces of constant sigma coordinates and (3) no longer applies (compare Fig. 2a and c).

For a two-dimensional case, the horizontal gradient of pressure in Cartesian coordinates, when evaluated on the VQS grid (which are not level surfaces), is

$$\left.\frac{\partial p}{\partial x}\right)_z = \left.\frac{\partial p}{\partial x}\right)_k - \left.\frac{\partial p}{\partial k}\frac{\partial k}{\partial x}\right)_z. \tag{4}$$

On VQS coordinates, as in sigma coordinates, the horizontal gradient of pressure is evaluated as the pressure gradient along a fixed kth layer (the first term on the right-hand side of (4)) and the

"hydrostatic correction" (the second term), which is proportional to the slope of the vertical layers. Analogous to the computation on sigma coordinates, the truncation error in the calculation of the pressure gradient is a function of the slope of the layers. When the layers are horizontal, the second term is zero and so is the error. Thus, the smaller slopes of the vertical layers in the VQS grid should lead to smaller truncation errors in the calculation of the horizontal pressure gradient.

4.2. Model test runs

Several metrics have been suggested to estimate truncation errors in sigma models (Haney, 1991; Mellor et al., 1994, 1998). The utility of Haney's parameter (1991) has been critiqued in Mellor et al. (1994, 1998) that instead suggest analytically derived metrics for Sigma Errors of the First and Second Kinds (SEFK and SESK, respectively). The analytical forms of these metrics are not applicable to the VQS grid because this grid is not truly based on sigma coordinates and an analytical relation between sigma surfaces and vertical layers is not tractable. To evaluate the performance of VQS coordinates within a numerical model and to compare with a classic sigma grid, idealized numerical tests using a suite of test model runs within the high-resolution SE domain described in Section 3.3 are conducted.

For the test experiments, the NCOM SE model domain is configured with three different vertical grids: 80 evenly spaced non-vanishing (or classic) sigma (NVS) layers computed by (2), 40 evenly spaced NVS layers, and 80 VQS layers computed as described in Section 3.2. Hence, these experiments allow comparison of the performance of the new VQS vertical grid, which is used for realistic simulation of the deep currents in the following sections, to the classic sigma vertical grid. Each model is initialized at rest with horizontally homogeneous density fields derived from long-term-average density profiles for the region from Conkright et al. (1998). The experiments are run prognostically for 20 days with no forcing at the surface or boundaries. The theoretical solution is that the ocean remains at rest with no change in the density field.

4.2.1. Slopes of vertical coordinate surfaces

In general, the slopes of the near-bottom vertical layers in the model with VQS coordinate are noticeably less steep over the SE than in the model with 80 and 40 NVS layers which has similar slopes of the sigma layers (Fig. 3, 40 NVS case is not shown). Over the upper SE, the VQS grid has remarkably reduced slopes of the vertical layers with a maximum slope of 0.1 (Fig. 3d), which is one-third smaller than in the NVS grids (Fig. 3b), but the maximum slopes in the VQS grid (Fig. 3c) are nearly the same as in the NVS grid over the lower SE (Fig. 3a). In the VQS model, however, large slopes are confined to several grid cells near the bottom over the steepest part of the escarpment, while in the NVS models, large slopes are found throughout the water column over a wider range of the sloping bottom. Thus, in the VQS grid, the upper layers are not substantially inclined due to the steep bathymetry underneath and the coordinate surfaces are nearly horizontal in the upper ocean where the strong vertical density gradients occur (compare Fig. 2a–c).

As discussed in a number of papers (e.g., Auclair et al., 2000), sharp density gradients, when associated with inclined vertical coordinate surfaces, lead to large truncation errors in the computation of the pressure-gradient term. In the NVS models, sigma layers preserve distinguishably non-zero slopes to above 1000 m over the upper SE. Doubling the number of vertical layers in NVS models does not reduce the slopes of the vertical layers, suggesting that addition of sigma layers does not reduce the error, in agreement with Mellor et al. (1994).

Parameters in the algorithm generating the VQS grid are chosen such that the layers vanish more rapidly, providing smaller slopes, over the upper SE than over the lower SE. This choice is dictated by the assumption that regions with weaker stratification (lower SE) can better tolerate greater slopes of the vertical layers than regions with stronger stratification (upper SE) (Auclair et al., 2000).

4.2.2. Density anomalies

From (4), truncation errors depend on the pressure gradient across the vertical coordinate surfaces $\partial p/\partial k$ (which, in the case of classic sigma coordinates, is equivalent to $\partial p/\partial\sigma$). At the resting

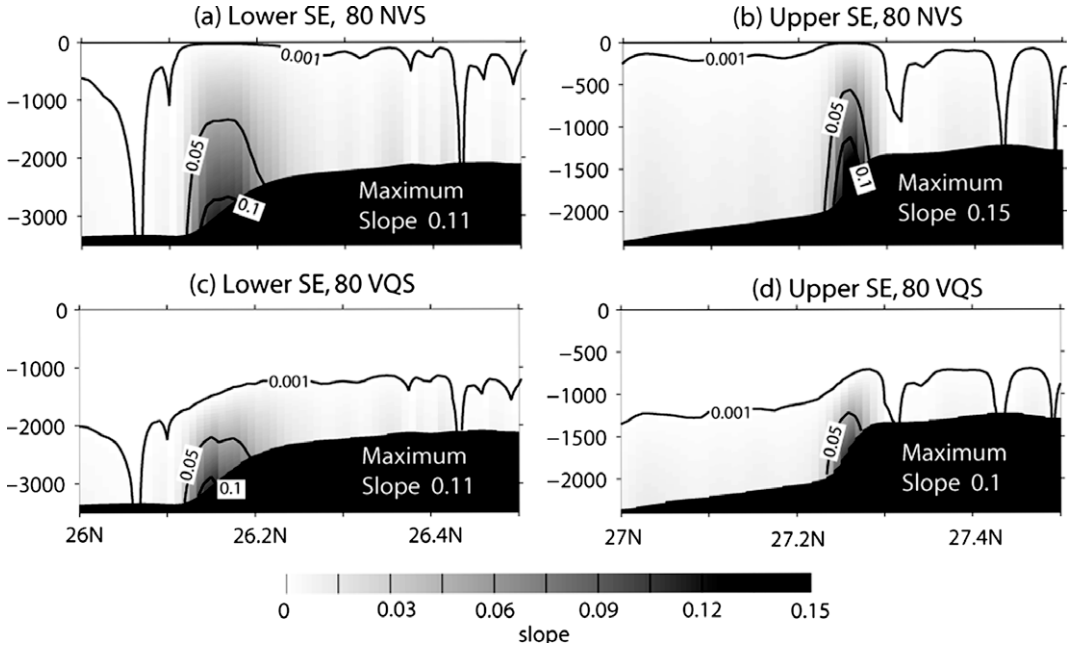

Fig. 3. Cross-sections of slopes of vertical coordinate surfaces. The cross-sections are at the lower (left column) and upper (right column) SE along 90.97°W and 89.93°W, respectively. The upper row (a and b) is from the model with 80 non-vanishing sigma layers, and the bottom row (c and d) is for 80 VQS layers (configuration used for simulating the deep currents over SE).

initial state, the LHS of (4) is identically zero, so the first term on the RHS of (4) should be balanced by the second term on the RHS. Due to the truncation error, however, this balance is violated as the model integrates. After the first time step, the horizontal pressure gradient is no longer zero and the initially motionless ocean starts moving. Due to the resulting mixing and advection, the model density field becomes no longer horizontally homogeneous.

Cross-sections of the density anomaly (the initial density field is subtracted) after 20 days of integration (Fig. 4, the 40 NVS case is not shown since it is similar to the 80 NVS result) show that the density field in all the models has drifted from the initial density distribution and noticeable horizontal gradients have developed throughout the water column. In the models with 80 (Fig. 4a) and 40 NVS layers, strong horizontal density gradients develop over the lower SE to a height of 1000–1500 m above the bottom. The experiment with the VQS grid (Fig. 4c) preserves better horizontal homogeneity of the density fields, although weak anomalies are developed near the lower SE slope. At the upper SE, the density fields of the NVS-grid-model experiments reveal strong horizontal inhomogeneity with maximum anomalies developed over the escarpment (Fig. 4b). The model with VQS layers has weaker horizontal density gradients over the upper SE with remarkably small gradients at its steepest part (Fig. 4d). It is noteworthy that in the model with the NVS grid, the maximum density anomalies occur in the surface layer, where the VQS grid model develops only small anomalies during the test run.

4.2.3. Maximum speeds

In the models with the NVS grid, non-zero velocities arising from truncation errors in the horizontal pressure-gradient calculation are largest near the upper and lower SE (Fig. 5a and b, only 80 NVS case is shown). After 20 days of the simulation, the maximum speed over the lower SE (0.08–0.10 m s^{-1}) is roughly one-third of the maximum speed over the upper SE (0.25 m s^{-1}) in these experiments. This is because the stratification at the upper SE is stronger, resulting in larger truncation errors and, thus, larger density anomalies, while the slopes at the cross-sections shown are comparable. Over the upper SE in the NVS-grid experiments, these spurious velocities have magnitudes roughly 2.5 time greater than the mean near-bottom speed measured in this area (~0.1 m s^{-1}) and reach nearly one-half of the maximum deep current (~0.5–0.6 m s^{-1}) observed at the MMS moorings over the upper SE in 2003–2004 (Donohue et al., 2006). At the lower SE, speeds resulting from truncation errors (0.08–0.1 m s^{-1}) are comparable to the observed mean (~0.1 m s^{-1}). Thus, it would be problematic to use this model with sigma coordinates to produce accurate simulations of the deep currents over the SE.

Large velocities in the NVS-grid-model experiments appear in the lower water column from the upper SE through the eastern part of the lower SE (Fig. 6a and b). It is worth mentioning that increasing the number of vertical layers does not reduce the erroneous velocities, as the maps of speeds near the bottom look similar in the models with 80 and 40 sigma layers. These velocities are a manifestation of the case when the Sigma Error of the First Kind (Mellor et al., 1994) is dominated by the change in water-column depth between grid points and is not sensitive to the number of vertical layers.

The smaller slopes of the vertical coordinate surfaces in the VQS grid result in much weaker and more localized deep currents over the lower and upper SE (Figs. 5c and d, 6c) compared to the NVS cases. Over the upper SE, speeds are less than 0.1 m s^{-1}, except for at several grid points very close to the escarpment where speeds reach a maximum of 0.11–0.12 m s^{-1}. In the VQS model, spurious velocities remain very small in amplitude ($\leqslant$0.02 m s^{-1}) across most of the slope of the lower SE, with a maximum speed of 0.05 m s^{-1} occurring 600 m above the shallower part of the lower SE.

Time series of the maximum (Fig. 7, upper row) and spatially-averaged (Fig. 7, bottom row) speeds are computed over the eastern parts of the lower (91.5W–90.8W) and upper (90.5W–89.8W) SE for the deepest layer at each grid point for the three model experiments. Domains for spatial averaging are defined by the −1500 and −2000 m isobaths at the upper SE, and the −2500 and −3000 m isobaths along the lower SE. These metrics show clearly the utility of the VQS grid. The maximum speeds resulting

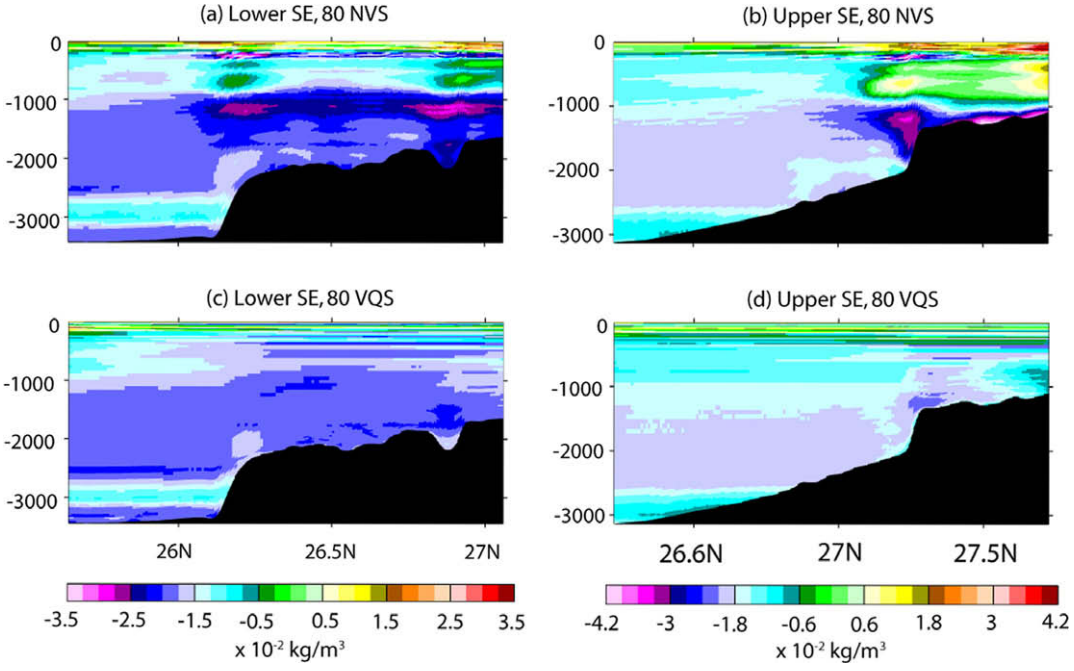

Fig. 4. Cross-sections of density anomalies developed from day 0 to day 20 of the test run in the models with different configuration of the vertical coordinates. The cross-sections are at the lower (left column) and upper (right column) SE along 90.97W and 89.93, respectively. The upper row (a and b) is the model with 80 NVS layers, and the bottom row (c and d) is from the model with 80 VQS layers.

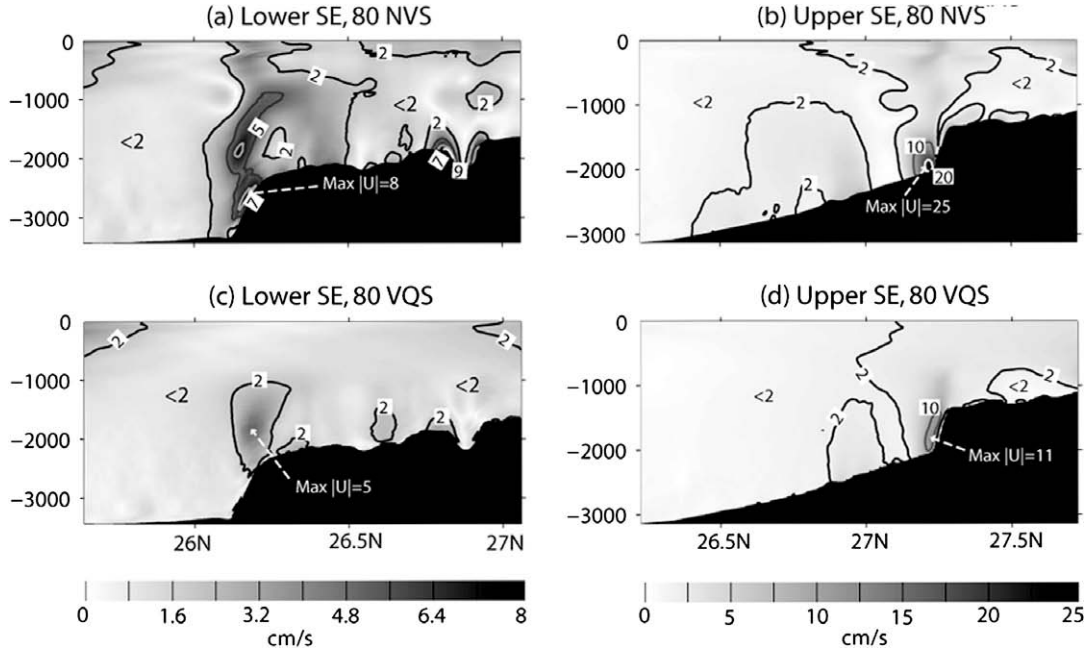

Fig. 5. Cross-sections of speeds resulting from truncation errors in the calculation of horizontal pressure gradient in the models with different configuration of the vertical coordinates. The cross-sections are at the lower (left column) and upper (right column) SE along 90.97W and 89.93W, respectively. The upper row (a and b) is the model with 80 NVS layers, and the bottom row (c and d) is from the model with 80 VQS layers. Note different scales for the Lower and Upper SE. "Max |U|" indicates values of maximum speed over the Escarpment.

from truncation errors are several times smaller in the model with the VQS grid than in the NVS-grid models. The difference is more noticeable over the upper SE (Fig. 7b) where the maximum speed in the model with the VQS is about 0.05 m s^{-1} while in the models with NVS grids the maximum speed is 0.15–0.18 m s^{-1} for 80 layers and 0.21–0.23 m s^{-1} for 40 layers.

An interesting detail seen in Fig. 7 is slower spurious currents simulated in the bottommost grid cell of the 80-layer NVS-grid model compared to the 40-layer model. This difference is not noticeable in the plot of the maximum speed computed over the 200-m thick near-bottom layer (Fig. 6). A possible explanation is that the bottommost grid cell in the 80-layer model is thinner and does not extend as high off the bottom as the bottommost grid cell in the 40-layer model. Note that the drag coefficient is inversely proportional to the logarithm squared of the grid cell thickness (Eq. (1)), resulting in greater drag in the bottommost grid cell in the 80-layer model compared to the 40-layer model.

Average speeds in the near-bottom layers over the SE in the VQS coordinate model are small, remaining less than 0.02 m s^{-1} over the lower SE and 0.01 m s^{-1} over the upper SE (Fig. 7c and d). In the VQS models, both maximum and mean currents driven by truncation errors stabilize or have a slight positive trend after 20 days of integration. In the NVS models, maximum speeds maintain small positive trends through the integration and do not tend to asymptote, except for the mean spurious speeds over the upper SE (Fig. 7d) where mean currents rapidly reach a peak value (0.035–0.04 m s^{-1}) and then level out. These tests demonstrate that implementation of the VQS vertical coordinate system in a numerical model of the SE region substantially reduces spurious currents arising from truncation errors so that this type of model can reasonably be used to simulate the intense near-bottom currents in the region.

5. Realistic simulation of deep currents over the Sigsbee Escarpment

The nested modeling system is applied as described in Section 3.3 to simulate energetic near-bottom currents over the SE with characteristics consistent with observations. The nested modeling system consists of the 1/120° SE domain obtaining initial and boundary conditions from the outer 1/20° GoM domain. First, the outer GoM domain is integrated for 10 years and the output analyzed to identify time periods of strong, deep currents over the SE.

Similar to observations (Donohue et al., 2006), the GoM model simulates two regions with strong currents over the SE. At the eastern end of the lower SE, the maximum speed over the 10-year period of integration is 0.59 m s^{-1} (Fig. 8a). Over the upper SE, a local maximum of 0.38 m s^{-1} is simulated during the model experiment. This intensification of the near-bottom currents over the SE, although relatively strong for such depths, is somewhat weaker than has been observed. One possible reason is that the 1/20° grid spacing of the GoM domain cannot adequately resolve the small spatial scales of the intensified currents or of the escarpment. The nested model approach refines the grid to allow the model to more accurately resolve these large topographic and velocity gradients necessary for properly simulating the strong current events.

Several times during the 10-year simulation, the SE region is directly impacted by energetic mesoscale eddies. Based on previous studies, it is expected that stronger near-bottom currents over the SE are more likely to occur during these times. One year of the outer-domain simulation is selected for a one-year nested model simulation. For this case study, relatively strong currents are simulated in the GoM model domain over the SE when the Loop Current has penetrated far to the northwest and separates a Loop Current Eddy, centered just southeast of the SE. During this year, several energetic, near-bottom, current events are evident in the GoM model domain over the upper SE, with a maximum current speed of 0.34 m s^{-1} over the upper SE and ~0.3 m s^{-1} over the lower SE. The high-resolution SE model is initialized from fields interpolated from the GoM domain at the first day of the case study and integrated for 365 days with boundary conditions being obtained from the GoM domain every 48 hours and output being saved every 6 hours. A series of analysis methods are applied to the model output for comparison with observations.

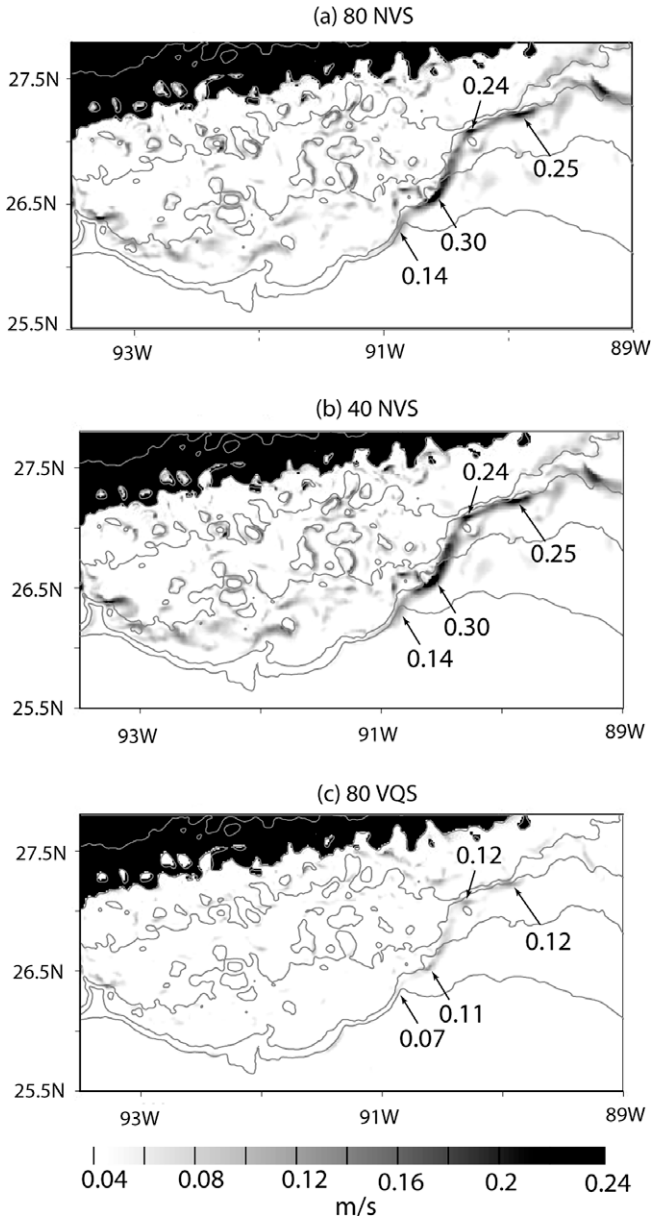

Fig. 6. Maximum speed in the lower 200 m after 20 days of the test runs of the models with different vertical discretization (a) 80 NVS levels; (b) 40 NVS levels; (c) 80 VQS levels. Speeds shallow than −1000 m are not shown. Isobaths are drawn every 500 m starting at −3500 m. Values of local maxima are shown.

5.1. Extreme near-bottom currents

Compared to the coarser-resolution GoM domain, the high-resolution SE nested model simulates much stronger currents along the SE (Fig. 8b). The intensification of the near-bottom currents is more clearly localized along the escarpment. Locations of the near-bottom maxima are similar to observations (Section 2.2). The most energetic near-bottom (in the lower 250 m) currents over the upper SE are simulated near the I2 mooring location (0.81 m s^{-1}) and at the southwestern side of Green Knoll (0.98 m s^{-1}). The maximum near-bottom current speed simulated within the nested domain is 1.17 m s^{-1} and occurs over the lower SE. Along the Escarpment, currents are most intense along the convex contours of the isobaths (appearing similar to capes in a coastline), while concave contours appear to be "shaded regions" where speeds are diminished. Thus, current speeds at two nearby locations along the escarpment may be drastically different (this feature has been noticed from observations and studies cited in Section 2.2). The existence of such extreme currents (and even more intense currents) at the upper SE is supported by observations (Hamilton and Lugo-Fernandez, 2001). At the lower SE, the MMS moorings did not measure currents stronger than 0.7 m s^{-1} during a one-year interval. This should not cast doubt on the model results because one year of observations at the lower SE may not be long enough to catch extreme events, which are very episodic. During the MMS observations, no extreme events occurred in the area (Donohue et al., 2006).

5.2. Mean current speeds

Mean deep currents computed from the one-year nested model simulation have similarities with the observations collected in the region (Section 2.2). A map of the modeled, mean, near-bottom speed (Fig. 8c) shows two distinct regions: one with quite weak (<0.1 m s^{-1}) flows located over shallower depths to the north of the escarpment (except for the western part where more energetic mean currents are simulated), and the other with more energetic currents along the escarpment and over deeper waters. Along the Escarpment are a few localized regions with mean current speeds greater than 0.2 m s^{-1}. One appears at the eastern end (around 91°W) of the lower SE with a mean speed of ~0.3 m s^{-1}. The upper SE is almost quiescent with speeds below 0.1 m s^{-1}. At the bottom of the slope, the mean currents are 0.13–0.18 m s^{-1}. An intensification of the mean currents up to 0.2 m s^{-1} is simulated at the eastern end of the upper SE where the isobaths converge.

Interestingly, the area to the southwest of Green Knoll has very weak mean currents (<0.1 m s^{-1}), which does not correspond to the map of maximum speeds (Fig. 8b) where very energetic flows are simulated. Inspection of an animation of the near-bottom speeds reveals that, except for one very energetic event, this area is shaded by the knoll, which obstructs the predominant flow along the escarpment from the east. Near the I2 mooring location, strong flows are more frequent, resulting in higher mean currents (although the simulated maximum speed is smaller at I2 than at Green Knoll). Intensification of the currents to the northwest and southeast of Green Knoll indicates flow intensifying as it is directed around the topographic feature.

5.3. Mean velocity vectors and standard deviation ellipses

Velocity vector means and standard deviations are computed for select grid points over the SE region (Fig. 9). Along the lower and upper SE, the mean current has a well-pronounced westward component. The standard deviations (STD) of the mean vectors, displayed as ellipses at the heads of the vectors, characterize the variability of the mean currents at the given locations. Variability of the simulated mean current vectors agrees well with characteristics of the measured currents (discussed in Section 2.2 and Donohue et al. (2006)). The prominent feature of the STD ellipses in the model is the along-isobath orientation of the major axes along the SE where the isobaths converge, which is indicative of quasi-rectilinear behavior of the currents over the steep slope. Over the flatter regions, the ellipses are more circular with their major axes rotated at a larger angle with respect to the isobaths. The semi-major axes of the ellipses are comparable in magnitude to the mean vectors. This shows that the simulated currents at the upper and lower SE are highly variable. The velocities range from near-zero to very strong currents directed westward along the isobaths. The STDs of the model vector velocities suggest that flows rarely reverse in this area.

5.4. Vector velocity time series

Time series of the simulated currents from the high-resolution nested model domain (Fig. 10) are analyzed for selected points

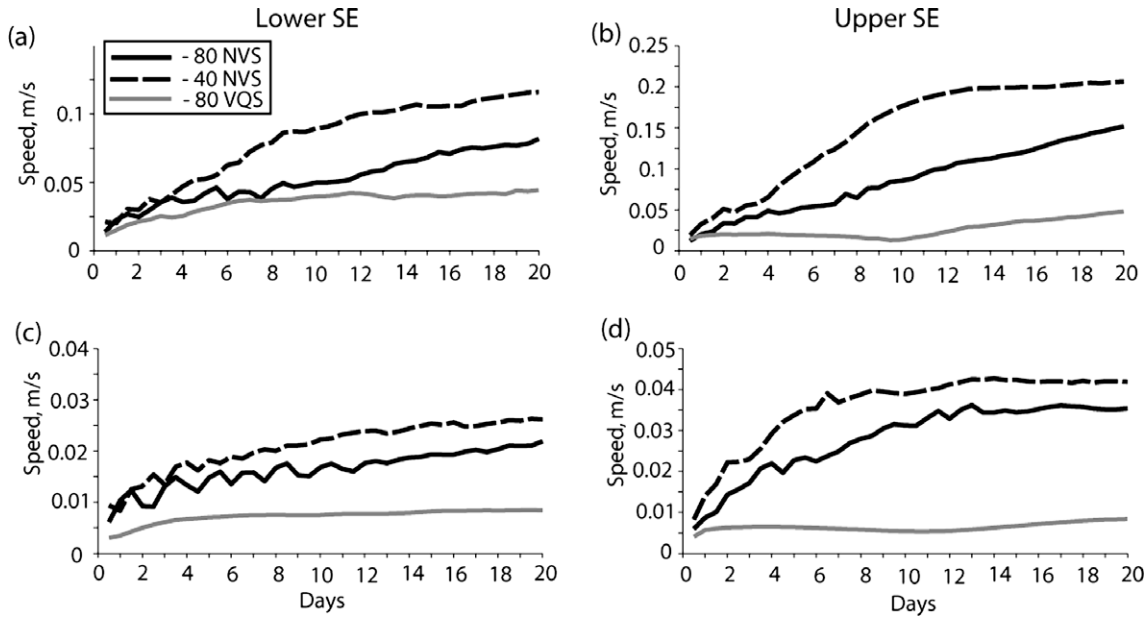

Fig. 7. Time series of the maximum (upper row) and spatially-averaged (bottom row) speeds over the Lower (left column) and Upper (right) SE for test model runs with 3 different vertical grids: 80 non-vanishing σ layers ("80 NVS"), 40 non-vanishing σ layers ("40 NVS"), and 80 vanishing (quasi) σ layers ("80 VQS"). The speeds are for the near-bottom coordinate surface.

across the lower and upper SE. The points are chosen in the middle of the escarpment along 90°W at the upper SE and 91°W at the lower SE. These points are located in the areas with high maximum near-bottom speeds (see Fig. 8b). For each grid point, vector time series are plotted showing currents at 90 m below the surface and approximately 800, 250, and 50 m above the bottom. These time series have many similarities to velocity time series collected during the MMS observational study discussed in Section 2.2:

- In the model, the near-surface and lower-layer vectors show no relationship, meaning that the upper- and lower-level flows are not coherent. Currents are coherent in the lower water column.
- Currents are intensified towards the bottom.
- Due to the frictional bottom boundary layer, the maximum flow in the lower water column is separated some distance above the bottom. In the model experiment, the maximum of the current speed during the most energetic events occurs at approximately 200–400 m above the bottom.

A noticeable difference between the simulated deep currents and the observations at the I2 mooring location is a more persistent westward orientation of the velocity vector in the model. Recorded current vectors exhibit rotational behavior and more frequently change direction from westward to eastward (compare Fig. 10b with Fig. 2 in Hamilton and Lugo-Fernandez, 2001). Unfortunately, at this stage it is impossible to state whether this difference is related to artifacts of the simulation or differences in the dynamical regimes from this one-year simulation and the time period of the observations.

Time vs. depth diagrams of speed (Fig. 11) more clearly demonstrate features noted from the velocity time series. The diagrams show that extreme events are episodic and not regular at the SE. The lower SE (Fig. 11a) has more strong events over the simulation (during days 80 through 180 of the integration and a single event around day 310). The upper SE (panel b), has a single strong event (occurring over a short time period centered near day 125) and several less energetic episodes. Both at the lower and upper SE, the deep currents are decoupled from the upper ocean. Intensification of the near-bottom currents is typically seen with only modest speeds at the surface. The time vs. depth diagrams of speeds of the simulated currents vividly demonstrate near-bottom intensification of the flow and the existence of shear due to the bottom boundary layer. Along both the lower and upper SE, the current is intensified a few hundred meters above the bottom and then slowly decays towards the upper ocean (above the main ocean thermocline, very intense currents are associated with upper-ocean circulation features).

The simulated currents at the upper SE have fairly good resemblance to observed oscillations at the I2 mooring during the strong event (compare panels a and b in Fig. 12). Both time series show shear near the bottom, likely due to the bottom boundary layer, with flow intensification at 200–400 m above the bottom. The dominant period of the observed oscillations is approximately 10 days, which matches noticeably well with the model results. In the simulated time series, the 10-day oscillation seems to be superimposed over a slower mode.

5.5. Wavelet analysis

Analyses of the observations reveal that the dominant periodicity of the low-frequency signal in the deep-ocean currents over the SE is 10–40 days (Donohue et al., 2006). The time series of the simulated currents are analyzed to estimate the time scale of the variability of the deep-ocean dynamics in the model. The velocity time series from the one-year simulation are nonstationary. The oscillations do not reveal a robust periodicity throughout the record. Thus, applying a wavelet transform to the time series aids in analyzing periodic behavior of the variability of the near-bottom currents over the escarpment.

The along-isobath velocity component is transformed using the Morlet wavelet (Goupillaud et al., 1984):

$$g(t) = c_\omega \pi^{-1/4} e^{-t^2/2} (e^{i\omega t} - e^{-\omega^2/2}) \tag{5}$$

where c_ω is the normalization constant:

$$c_\omega = (1 + e^{-\omega^2} - 2e^{-3\omega^2/4})^{-1/2}. \tag{6}$$

To reduce ringing, each end of the time series is extended by adding a trigonometric taper $(1 - \sin\phi)$ where ϕ is chosen such that the taper vanishes over the extended interval (100 days).

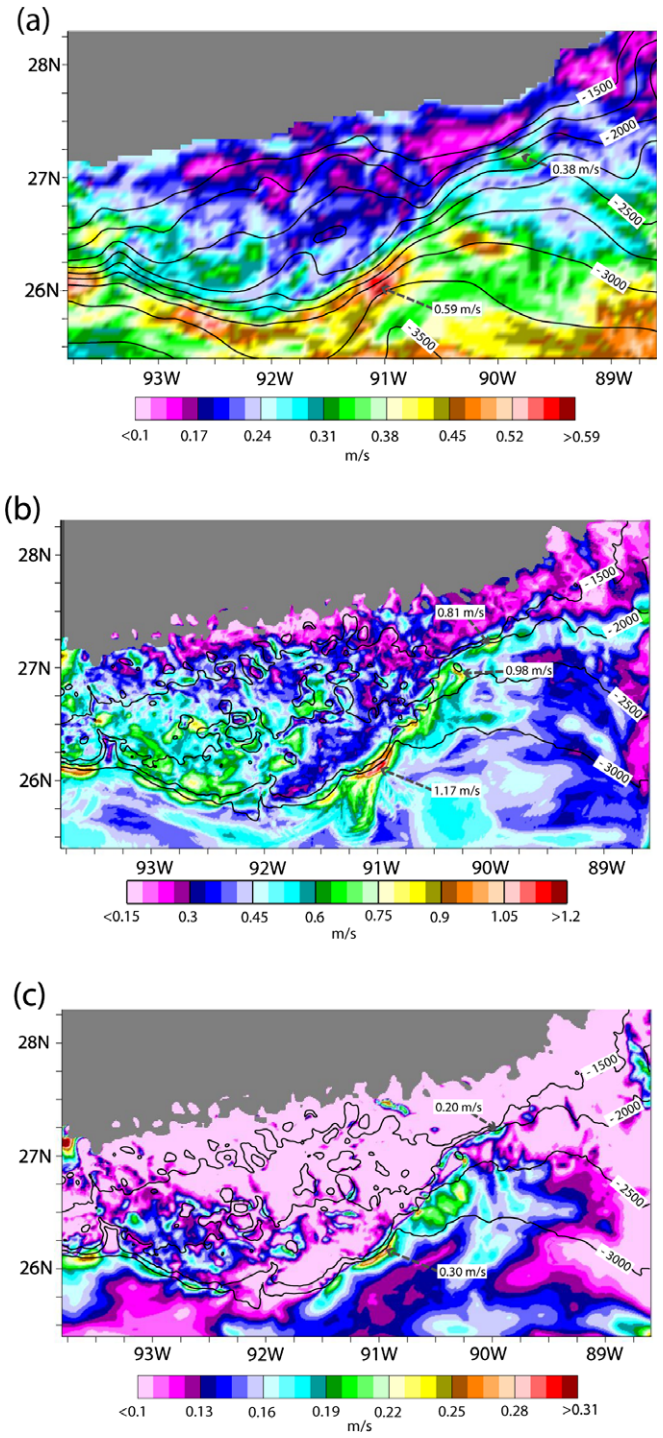

Fig. 8. (a) Maximum near-bottom (lower 250 m) speed over the SE region during 10 years of the GoM model run. The arrows indicate locations of local speed maxima over the 10-year integration at the lower and upper SE. The grey area is where the seafloor is shallower than −1000 m. (b) Maximum near-bottom (lower 250 m) speed over 1 year of the SE model run. (c) Near-bottom speed averaged over 1 year of the integration.

Over the lower SE, the wavelet transform indicates oscillations of a more complex nature (Fig. 13a) than those at the upper SE (Fig. 13b). Over the deeper SE, the oscillations are less regular and persistent with frequency rapidly shifting higher and lower. Prior to model year-day 120, the site is influenced by two wave patterns: one with low-frequency motions with periods of 70–90 days, and the other with higher-frequency oscillations of approximately 20-day periodicity. These faster oscillations are more prominent at the lower SE than at the upper SE. After about 130 days of the nested model run, the frequencies of the fast and slow modes begin to converge and the dominant periodicity gradually shifts to 35–65 days by day 200. During days 210–270, there are two prominent, although weakened, modes of oscillations with more-defined periodicity (the maxima are more localized). The slower mode shows 45–60 day periodicity, dissipating toward the end of the integration, and faster oscillations of about 20-day periodicity are well identified in the diagram.

For the upper SE, the wavelet diagram (Fig. 13b) reveals a dominant wave pattern with the period of oscillation ranging from 35 to 65 days. This pattern is surprisingly distinct and robust throughout the simulation. The frequency of these oscillations only slightly drifts lower during the simulation. The maxima of the wavelet transform coefficients are well localized in this frequency interval, meaning that these oscillations are regular and should be easily identifiable by spectral analysis. There are also a clear, slowly-oscillating mode (100–120 days) and weak oscillations with 10–30 day period. The slowly-oscillating pattern may be associated with slow changes in the character of the upper-ocean mesoscale dynamics. The period of the faster modes (~10 and 30 days) agrees with the observed periodicity in the area (Donohue et al., 2006). It should be noted that this faster mode intensifies during the time period that intense currents are simulated in the area near model year days 110–130. Similar 10-day oscillations are observed in the time series of the speed of the recorded currents at the I2 mooring (Fig. 12b).

The wavelet analysis of the nonstationary velocity time series identifies differences in the character of the oscillations between the upper and lower SE, and identifies multiple modes of oscillation. The periodicities of the oscillations tend to shift during the year-long integration, but the relatively fast modes are evident throughout. The enhancement of the amplitude of the fast oscillations during the most energetic events is consistent with previous studies and adds to the confidence that the model is indeed reproducing the observed dynamics over the escarpment.

6. Discussion and conclusions

This modeling effort was motivated by a series of observations of extreme deep currents over the SE. The physical phenomenon responsible for the intense near-bottom flows has not yet been fully explained and requires a comprehensive (observational, analytical, and numerical) investigation for the benefit of both scientific and engineering applications. This study is the first known attempt to simulate extreme near-bottom currents over the SE with a numerical model. A new VQS vertical grid has been developed to overcome difficulties faced by traditional ocean models for studying deep currents over a region with such complicated topography and steep slopes. Model test experiments have demonstrated that the new vertical grid results in smaller numeric errors for the simulation over the steeply sloping bottom compared to a traditional sigma-layer model. Implementation of the new VQS vertical grid with up to 80 unevenly stretched vertical layers provides accurate representation of the SE slope and the highest (known to date) vertical resolution over the escarpment.

A nested modeling system has been developed for this study to adequately resolve the small spatial scales of the escarpment and the observed intense currents. With this approach, a very-high-resolution (approximately 800–900 m) model domain can be applied to the SE region, while still being influenced by realistic, upper-ocean, mesoscale circulation features of the Gulf of Mexico simulated by the outer nest. The dynamic fields simulated using this nested model approach have properties that agree well with the prominent features of the observed currents over the Escarpment (Sections 2.3):

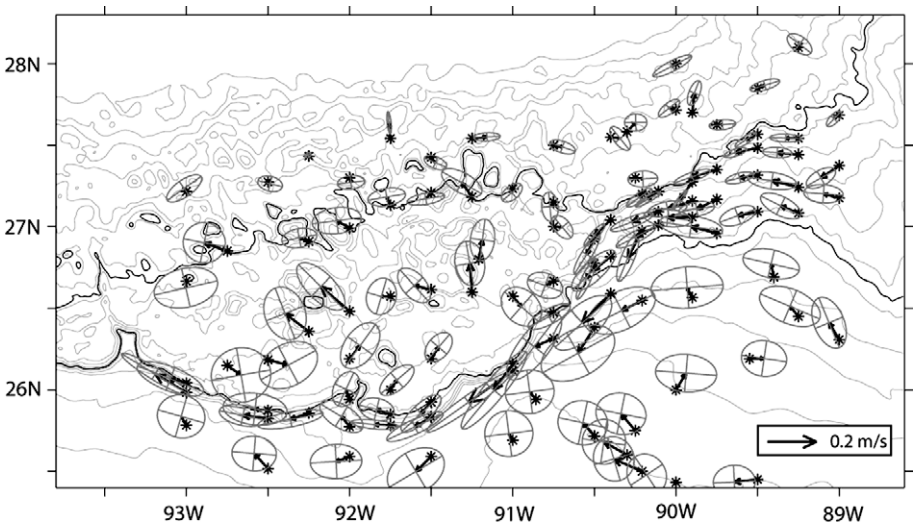

Fig. 9. Near-bottom mean velocity vectors and standard deviation ellipses over the SE estimated from 1 year of data from the Sigsbee Escarpment model. Locations of the mean vector estimates are marked with asterisks. Grey isobaths are drawn every 200 m, and the −1500 and −2000 m isobaths are shown by black contours.

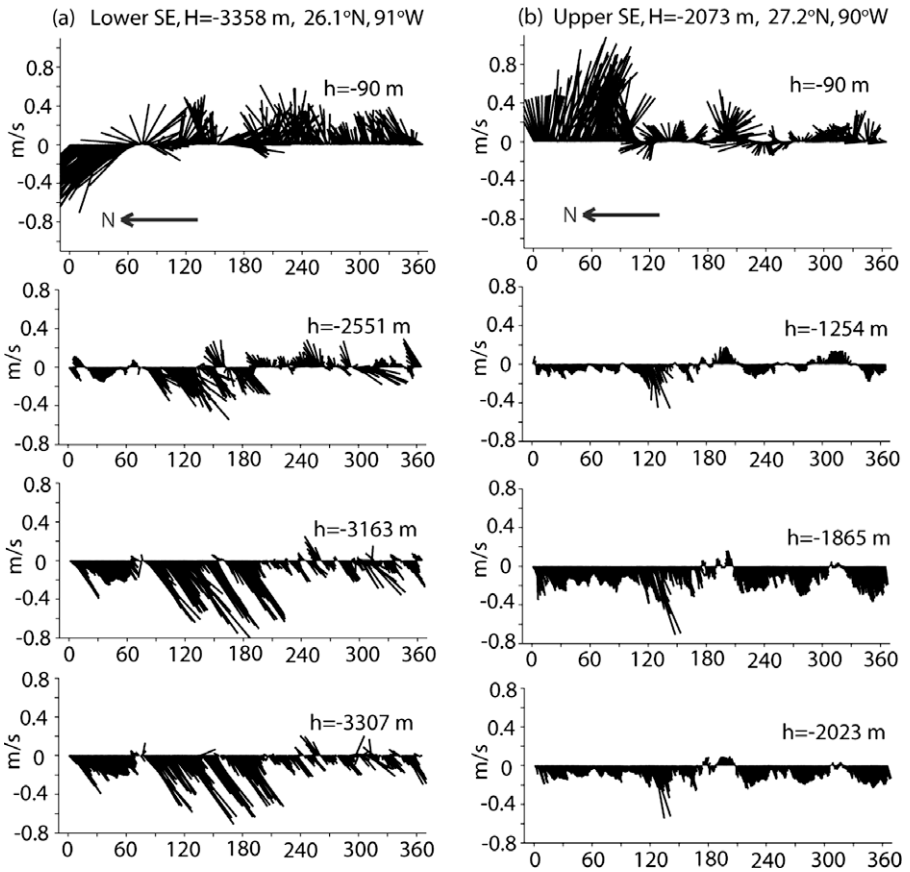

Fig. 10. Time series of daily velocity vectors for one year of the SE model run. The column (a) and (b) show velocity at grid points at the lower and upper SE, respectively (the coordinates are in the heading). The bottom depth and coordinates of the grid points are given in the headings. The horizontal axis is the model time in days. For each point, time series are presented at 4 depth levels indicated in the diagrams as "*h*". Note the orientation of the north direction shown in the upper panels.

Mean currents. Along the SE, the simulated, near-bottom, mean currents are directed predominantly southwestward with major axes of the STD ellipses oriented at small angles to the isobaths, indicating quasi-rectilinear oscillations. Speeds of the mean currents in the model range from 0.1 to 0.3 m s^{-1}. Currents are weaker over the shallower topography to the north of the SE (less than 0.1 m s^{-1}). Along the slope, intensification of the mean currents is observed at locations seemingly influenced by topographic irregularities along the lower and upper SE.

Extreme currents. Several events with intense near-bottom currents are simulated along the SE. The strongest currents are located near locations where similar extreme currents have been observed. At the upper SE, the strongest simulated speed is 0.81 m s^{-1}. Stronger speeds up to 1.17 m s^{-1} are simulated along the lower SE.

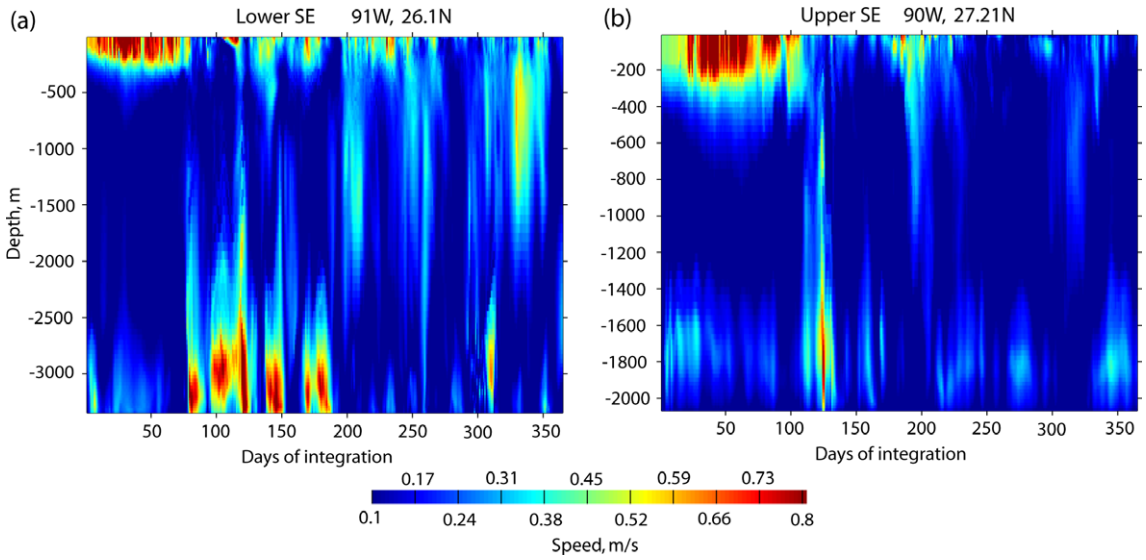

Fig. 11. Time (horizontal axis) vs. depth (vertical axis) diagrams of speeds of the simulated velocities at the lower (a) and upper (b) SE. Coordinates of the locations are indicated in the headings.

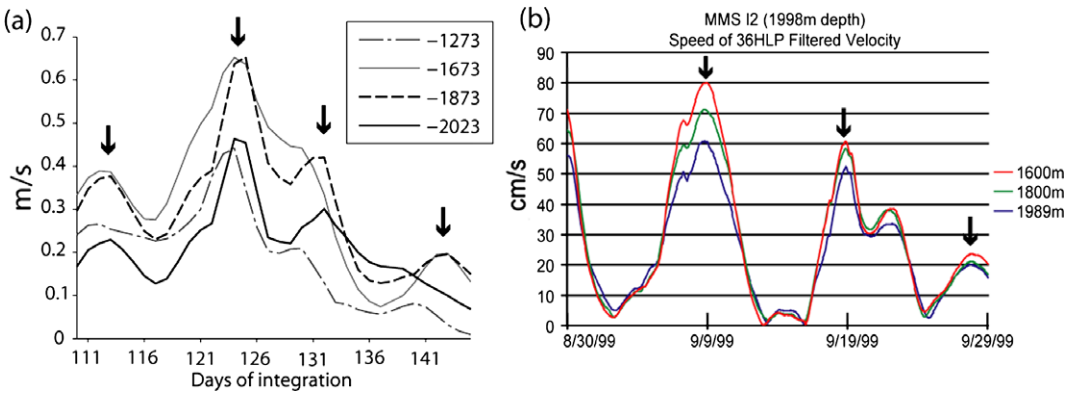

Fig. 12. Current speed at different depth levels in the model (a) and I2 mooring observations (b) at the upper SE. The model time series in (a) is 48 HLP filtered and the grid point is located close to the I2 mooring (90°W, 27.21°N, same as Fig. 11b). (b) Current speed of 36 HLP filtered velocity data from the I2 mooring. The arrows indicate peaks of a quasi-10-day period signal.

Periodicities of oscillations. From inspection of the time series of current speed and the wavelet analysis of the model velocity, the estimated periodicity of the low-frequency signal during strong events in the region is 10–30 days in agreement with observations. The slower modes of the simulated currents with periods 40–60 days observed in the wavelet diagrams can also be seen in some of the spectra from the Donohue et al. (2006) study. Analysis of the simulation suggests that these slow-oscillating modes are not attributed to the strong events.

The model development and evaluation described in this work is intended to produce a modeling methodology that can be applied to future studies of the dynamical aspects these extreme events over the SE. Nevertheless some preliminary results related to the dynamics of the deep currents over the SE from analyses of the model experiments can be mentioned here.

- The modeling results show dominantly quiescent conditions over the area, but with occasional strong events when an eddy migrates over the region, especially over the upper SE. This result agrees with observations that suggest a linkage between the near-bottom extreme events and intense eddy activity in the vicinity. However, some strong events are simulated over the lower SE away from the upper ocean eddy activity. Thus, the model results suggest the possibility for different genesis of the extreme events over the lower (local and remote genesis) and upper (local) SE.
- Strong events simulated over the SE appear to propagate. It is not clear yet whether the propagation of the strong currents along the slope is a manifestation of a topographically-trapped wave or a deep eddy impinging the slope. Both possibilities are supported by observations (Donohue et al., 2006). The applicability of Rhine's (1970) TRWs theory to the studied case should be revisited. The slope of the SE is steeper than slopes permitted in Rhines (1970) theory for TRW-like motion. Also, bottom friction is not taken into account in this theoretical description of TRWs.
- Directly over the SE, flows in the deep ocean are predominantly not coherent with flows at the surface.
- Simulated strong events are localized (in agreement with observations, e.g., Hamilton, 2007), suggesting that there are certain areas along the escarpment favored for flow intensification.
- The maximum speed of the modeled flows is achieved at some height (~100–200 m) above the bottom, which suggests the influence of the bottom boundary layer on the vertical structure of the extreme currents.

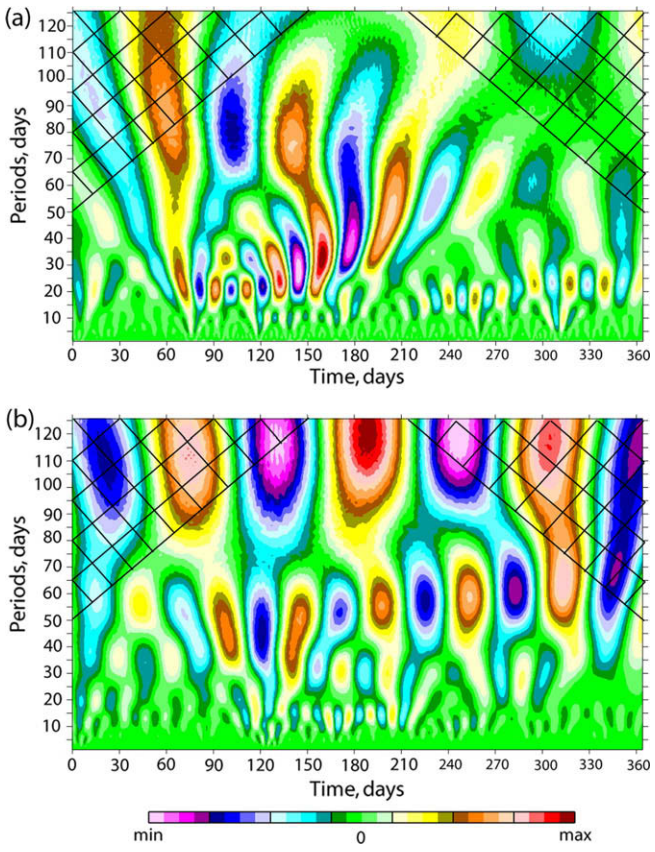

Fig. 13. Morlet wavelet transform coefficients (amplitude) of the time series of the along-isobath component of the near-bottom (250 m above the bottom) velocity at the lower (a) and upper (b) SE. The location of the grid point at the upper SE is 27.2N, 90W, and at the lower SE is 26.1N, 91W. The mesh indicates the cone of influence at the endpoints, meaning the wavelet coefficients are not significant in that area. The colors represent values of the coefficients relative to the minimum and maximum. The vertical axis is the scale length of the wavelet converted into periods. The horizontal axis is the translation parameter describing the position of the wavelet on the time axis.

Although the results of the simulation demonstrate that the newly-developed model has met the goals of the study, the analysis of the numerical experiments highlights aspects of the model that potentially require further investigation and might yet be improved to achieve better simulations of the deep-ocean dynamics and bottom-intensified features over the SE. Of concern is the role that the ocean bottom boundary layer seems to play in altering the vertical structure of the bottom-intensified currents. More attention should be placed on accurately modeling the boundary layer by investigating the consequences of the turbulence closure scheme and the parameterization of bottom roughness. Changing parameters of the bottom friction drag coefficient (1) can affect the location of the maximum relative to the local bottom, though it is unlikely that it will drastically change the intensity of the current.

It is possible that the horizontal resolution of the SE regional model is still inadequate for accurately representing the steep topographic features and this should be addressed. The effect of the vertical resolution in the model on simulating the strong near-bottom current has not been thoroughly investigated. Finally, a hindcast simulation of a strong event needs to be performed to more directly compare the model results with the observations and validate the model. Nevertheless, this modeling methodology can be applied to significantly advance understanding the dynamics over the Sigsbee Escarpment region.

Acknowledgments

This study was funded by DeepStar. The authors would like to thank Alan Wallcraft at the Naval Research Laboratory for assistance with the model. We acknowledge the Florida State University shared High-Performance Computing facility and staff for contributions to results presented in this paper.

References

Auclair, F., Marsaleix, P., Estournel, C., 2000. Sigma coordinate pressure gradient errors: evaluation and reduction by an inverse method. J. Atmos. Ocean. Technol. 17, 1348–1367.

Chu, P.C., Fan, C., 1997. Sixth-order difference scheme for sigma coordinate ocean models. J. Phys. Oceanogr. 27, 2064–2071.

Conkright, M., Levi0tus, S., O'Brien, T., Boyer, T., Antonov, J., Stephens, C., 1998. World Ocean Atlas 1998 CD-ROM Data Set Documentation, Tech. Report 15, NODC Internal Report, Silver Spring, MD.

DaSilva, A., Young, A.C., Levitus, S., 1994. Atlas of Surface Marine Data 1994. Algorithms and Procedures, NOAA Atlas NESDIS 6, vol. 1. US Department of Commerce, Washington.

Donohue, K., Hamilton, P., Leaman, K., Leben, R., Prater, M., Watts, D.R., Waddell, E., 2006. Exploratory study of deepwater currents in the Gulf of Mexico, vol. II. Technical report, US Dept. of the Interior, Minerals Management Service, Gulf of Mexico OCS Region, New Orleans, LA, 430pp.

Dukhovskoy, D.S., Morey, S.L., O'Brien, J.J., 2006. Influence of multi-step topography on barotropic waves and consequences for numerical modeling. Ocean Modell. 14, 45–60. doi:10.1016/j.ocemod.2006.03.002.

Ezer, T., Arango, H., Shchepetkin, A.F., 2002. Developments in terrain-following ocean models: intercomparisons of numerical aspects. Ocean Modell. 4, 249–267.

Goupillaud, P., Grossman, A., Marlet, J., 1984. Cycle-octave and related transforms in seismic signal analysis. Geoexploration 23, 85–102.

Hamilton, P., 1990. Deep currents in the Gulf of Mexico. J. Phys. Oceanogr. 20, 1087–1104.

Hamilton, P., 2007. Deep-current variability near the Sigsbee Escarpment in the Gulf of Mexico. J. Phys. Oceanogr. 37, 708–726.

Hamilton, P., Lugo-Fernandez, A., 2001. Observations of high speed deep currents in the northern Gulf of Mexico. Geophys. Res. Lett. 28, 2867–2870.

Hamilton, P., Singer, J.J., Waddell, E., Donohue, K., 2003. Deepwater observations in the Northern Gulf of Mexico from in-situ current meters and PIES, Final Report, vol. II. Technical Report, US Dept. of the Interior, Minerals Management Service, Gulf of Mexico OCS Region, New Orleans, LA, 95pp.

Haney, R.L., 1991. On the pressure gradient force over steep topography in sigma coordinate ocean models. J. Phys. Oceanogr. 21, 610–619.

Hollister, C.D., Heezen, B.C., 1966. Ocean bottom currents. In: Fairbridge, R.W. (Ed.), Encyclopedia of Oceanography. Rheinhold Publishing Corp., New York, pp. 576–583.

Hunkins, K.I., Ewing, M., Heezen, B.C., Menzies, R.J., 1960. Biological and ecological observations on the first photographs of the Arctic Ocean deep-sea floor. Limnol. Oceanogr. 5, 157–161.

Leben, R.R., 2005. Altimeter-derived Loop Current metrics, circulation in the Gulf of Mexico: observations and models. Geophys. Monogr. Ser., 161. doi:10.1029/161GM15.

Martin, P.J., 2000. A description of the Navy Coastal Ocean Model Version 1.0. NRL Report: NRL/FR/7322-009962, Naval Research Laboratory, Stennis Space Center, MS, 39pp.

Mellor, G.L., Ezer, T., Oey, L.-Y., 1994. The pressure gradient conundrum of sigma coordinate ocean models. J. Atmos. Ocean. Technol. 11, 1126–1134.

Mellor, G.L., Oey, L.-Y., Ezer, T., 1998. Sigma coordinate pressure errors and the seamount problem. J. Atmos. Ocean. Technol. 15, 1122–1131.

Mihailović, D.T., Zanjic, Z.I., 1984. Comparison of methods for reducing the error of the pressure gradient force in sigma coordinate models. Meteorol. Atmos. Phys. 35 (3), 177–184. doi:10.1007/BF01026173.

Morey, S.L., Martin, P.J., O'Brien, J.J., Wallcraft, A.A., Zavala-Hidalgo, J., 2003. Export pathways for river discharged fresh water in the northern Gulf of Mexico. J. Geophys. Res. 108 (C10), 3303. doi:10.1029/2002JC001674.

Nowlin Jr., W.D., Jochens, A.E., DiMarco, S.F., Reid, R.O., Howard, M.K., 2001. Deepwater physical oceanography reanalysis and synthesis of historical data: Synthesis report. US Dept. of the Interior, Minerals Management Service, Gulf of Mexico OCS Region, New Orleans, LA. OCS Study MMS 2001-064. 530pp.

Oey, L.-Y., 1996. Simulation of mesoscale variability in the Gulf of Mexico: sensitivity studies, comparison with observations, and trapped wave propagation. J. Phys. Oceanogr. 26, 145–175.

Oey, L.-Y., Lee, H.-C., 2002. Deep eddy energy and topographic Rossby waves in the Gulf of Mexico. J. Phys. Oceanogr. 32 (12), 3499–3527.

Pequegnat, W.E., 1972. A deep bottom current on the Mississippi Cone. In: Capurro, L.R.A., Reid, J.L. (Eds.), Contributions on the Physical Oceanography of the Gulf of Mexico. Gulf Publishing Company, Houston, TX, pp. 65–87.

Reid, J.L., 1969. Preliminary results of measurements of deep currents in the Pacific Ocean. Nature 22, 848.

Rhines, P.B., 1970. Edge-, bottom-, and Rossby waves in a rotating stratified fluid. Geophys. Fluid. Dyn. 1, 273–302.

Rowe, G.T., Menzies, R.J., 1968. Deep bottom currents off the coast of North Carolina. Deep-Sea Res. 15, 711–719.

Shchepetkin, A.F., McWilliams, J.C., 2003. A method for computing horizontal pressure-gradient forcing in an oceanic model with a nonaligned vertical coordinate. J. Geophys. Res. 108 (C3), 3090. doi:10.1029/2001JC001047.

Skoda, J.D., 1970. A survey of literature pertaining to sediment transport on the deep-sea floor. In: Einstein, H.A., Wiegel, R.L. (Eds.), A Literature Review on Erosion and Deposition of Sediment Near Structures in the Ocean Floor. Hydraulic Engineering Laboratory, College of Engineering, Univ. of Calif., Berkley, Calif., pp. 1–39.

Stelling, G.S., Van Kester, J.A.T.M., 1994. On the approximation of horizontal gradients in sigma coordinates for bathymetry with steep bottom slopes. Int. J. Numer. Methods Fluids 18, 915–935.

Sturges, W., Leben, R., 2000. Frequency of ring separations from the Loop Current in the Gulf of Mexico: a revised estimate. J. Phys. Ocean. 30, 1814–1819.

Sturges, W., Lugo-Fernandez, A. (Eds.), 2005. Circulation in the Gulf of Mexico: Observations and Models. AGU, p. 347.

Thiem, Ø., Berntsen, J., 2006. Internal pressure errors in sigma-coordinate ocean model due to anisotropy. Ocean Modell. 12, 140–156.